Volume 6 | Number 37 | 7 October 2018 | Pages 17831–18328

Journal of Materials Chemistry A

Materials for energy and sustainability

rsc.li/materials-a

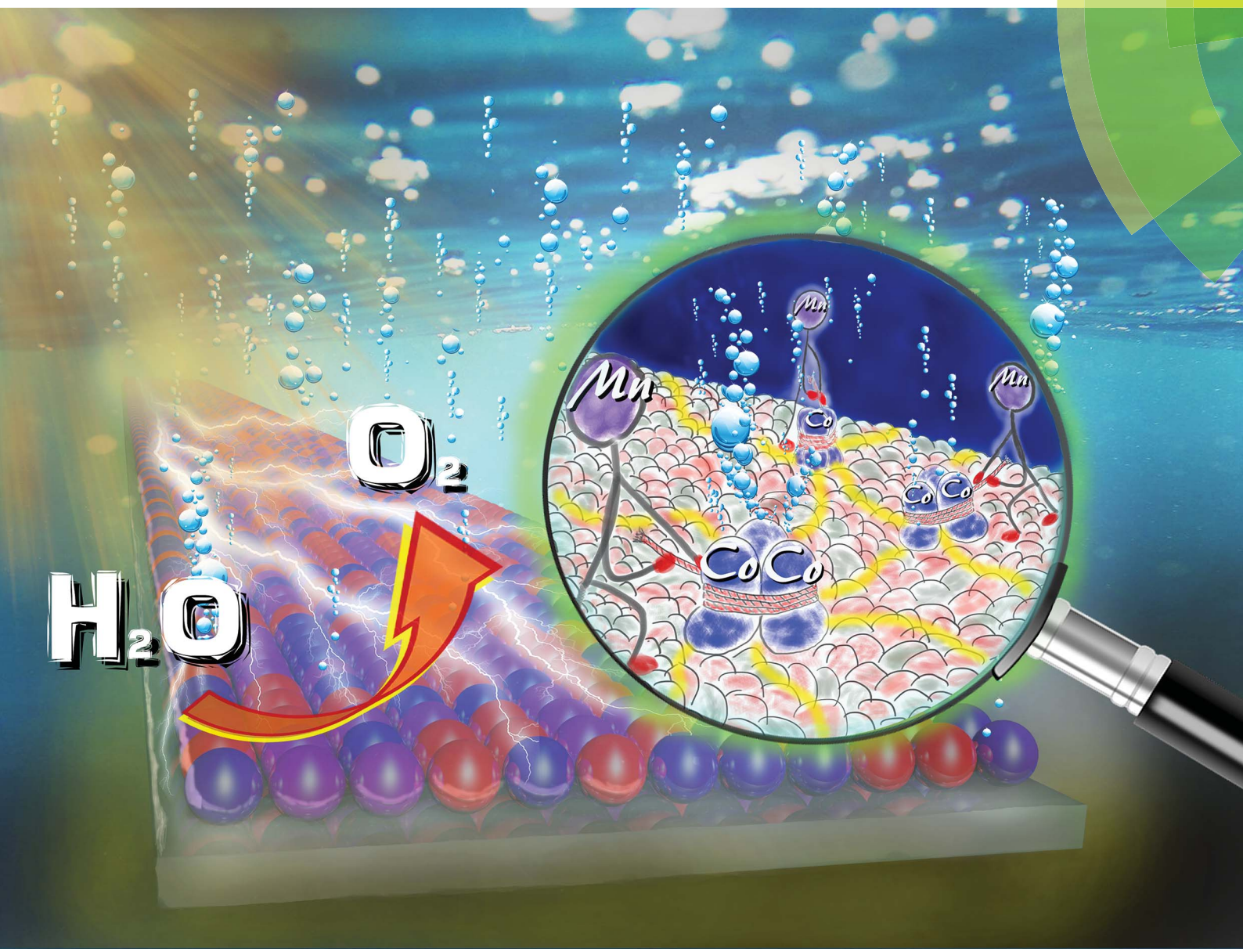

ISSN 2050-7488

ROYAL SOCIETY OF CHEMISTRY

PAPER

Chun-Hu Chen *et al.*

Redox-assisted multicomponent deposition of ultrathin amorphous metal oxides on arbitrary substrates: highly durable cobalt manganese oxyhydroxide for efficient oxygen evolution

Journal of Materials Chemistry A

PAPER

View Article Online
View Journal | View Issue

Cite this: J. Mater. Chem. A, 2018, 6, 17915

Redox-assisted multicomponent deposition of ultrathin amorphous metal oxides on arbitrary substrates: highly durable cobalt manganese oxyhydroxide for efficient oxygen evolution†

Ren-Huai Jhang, Chang-Ying Yang, Ming-Chi Shih, Jing-Qian Ho, Ya-Ting Tsai and Chun-Hu Chen *

Deposition of ultrathin multicomponent coatings (<10 nm) commonly encounters difficulties of discontinuous grains, elemental segregation, and specific limits of dimensions and physical properties of substrates. We present a large-scale, solution-processable deposition of metal oxides capable of introducing diverse elemental combinations (ternary oxides of Fe, Mn, Co) and conducting substrate-universal deposition (including non-conductive plastics) under aqueous conditions. The redox-coupled film growth of amorphous binary cobalt manganese oxyhydroxide (CMOH) results in homogeneous elemental distribution, strong film adhesion and integrity, lower sheet resistance (7.41 to 13.0 $\times$ 10^7 Ω sq^{-1}), and high visible light transparency (98.4%). The effects of deposition time, temperature, precursors, additives, and elemental ratios on film growth and compositions were investigated through cross-section, *in situ* growth monitoring, and elemental analysis. Experimental studies and molecular dynamics (MD) simulations reveal the strong dependence of film thickness on precursor anions, where acetate anions are responsible for achieving ultrathin deposition (6–10 nm). Amorphous CMOH shows higher OER activities (overpotential of 0.39 V) and more durable stability compared to its crystalline counterpart and benchmark RuO_2 (overpotential of 0.59 V). Various electrodes (Ni foam, carbon cloth, Cu foil, and glassy carbon) exhibit significantly enhanced OER performance with CMOH coating.

Received 13th June 2018
Accepted 2nd August 2018

DOI: 10.1039/c8ta05629c

rsc.li/materials-a

1. Introduction

Ultrathin multicomponent deposition (<10 nm) over large dimensions is of great interest to engineers and scientists, but it commonly suffers from island-like discontinuity and elemental segregation. Transition metal oxide thin films with uniform thickness and continuous coverage are shown to be essential in a wide range of modern devices and architectures, including flexible and wearable electronics.[1–3] Well-established chemical and physical depositions (*e.g.* chemical vapor deposition, evaporation, sputtering, atomic layer deposition, *etc.*)[4,5] require a high standard of operation conditions (*e.g.* delicate chemicals, high vacuum/energy consumption, expensive instrumentation, *etc.*) but provide limited production scales. Solution processable deposition, due to its low-cost and easy operation, emerges to explore low temperature,[6–8] massive-scale fabrication on substrates of low thermal-durability (plastics/soft materials) and complex 3D structures.[2,9] Many typical solution-processable depositions (*e.g.* drop-casting, sol–gel, spray/dip/spin coating, *etc.*) require pyrolysis to remove an organic residue and to promote film adhesion,[7,10–15] however, they are not suitable for amorphous/metastable deposition and soft/flexible substrates.[9] Electrodeposition may be considered as a substitute to avoid pyrolysis, but highly conductive substrates are generally needed. The drawbacks of pinhole formation, rapid deposition rates hindering ultrathin coatings, and inhomogeneous multi-element deposition due to varied deposition potentials for individual elements,[16,17] also limit its control in active site formation and charge transport resistance for electrocatalysis.[18,19]

Electrocatalytic water splitting to generate hydrogen and oxygen is a clean process crucial for energy storage of intermittent power sources (*e.g.* solar, wind, *etc.*).[20,21] Thin films of earth-abundant transition metal oxides with easy deposition are promising candidates to achieve efficient oxygen evolution reaction (OER) at a reasonable cost.[22–35] Notably, studies have shown that amorphous transition metal oxides, including intermediate states present during electrocatalysis, possess greater activities than their crystalline forms.[12,36–45] However, only a few examples of amorphous oxide coatings were successfully reported due to a pyrolysis step commonly involved in solution processable deposition. The Nocera group utilized *in*

Department of Chemistry, National Sun Yat-sen University, Kaohsiung, Taiwan 80424. E-mail: chunhu.chen@mail.nsysu.edu.tw

† Electronic supplementary information (ESI) available. See DOI: 10.1039/c8ta05629c

situ electrodeposition to generate amorphous cobalt-based electrocatalysts to execute the OER in neutral conditions.[36] Berlinguette and coworkers have demonstrated photochemical-assisted metal organic routes to produce amorphous coatings composed of mixed metal oxides active for the OER.[12,42]

Despite the promising OER activities, the high resistivity of an amorphous metal oxide is problematic in electrocatalysis. To improve the intrinsic conductivity and reduce the charge transport barrier, achieving multicomponent metal oxide coatings with mixed valence and homogeneous distribution is a highly challenging but effective strategy to enhance the electron hopping process and thus conductivities.[26,46–48] Ultrathin, highly continuous deposition of amorphous multicomponent metal oxides is therefore an optimal and desirable model for OER electrocatalysts.

In this work, we report a simple, scalable approach to realize ultrathin amorphous multicomponent metal oxide coatings on arbitrary substrates (including flexible plastics) under ambient conditions. The ultrathin coatings exhibit high continuity and elemental uniformity over a centimeter-scale surface with a thickness of 6–10 nm. As $KMnO_4$ is a strong stain reagent on various surfaces (*e.g.* fabrics, plastic, and even human skin), we were inspired to utilize this nature of $KMnO_4$ to achieve strong film adhesion on arbitrary substrates without pyrolysis treatment. $Co(OAc)_2$ and $KMnO_4$ interactions result in self-limited redox-coupled film growth governed by ligand coordination effects. For electrocatalytic OER applications, amorphous CMOH exhibits superior activities and durability to its crystalline counterpart and also benchmark RuO_2.

2. Experimental section

2.1. Preparation of CMOH thin films

The reaction mixtures for deposition were prepared by dissolving cobalt precursors (*i.e.* $Co(OAc)_2$, $CoSO_4$, and $Co(NO_3)_2$) (Showa) and $KMnO_4$ (J. T. Baker) in deionized (DI) water (18.2 MΩ cm) with a typical Co/Mn mole ratio of 3/1. As a substrate, we mainly used fluorine-doped tin oxide (FTO) glass obtained from Hartford Glass. FTO was rinsed with acetone, isopropyl alcohol (IPA), DI water, and 5.2 M HNO_3 under sonication for 10 min, followed by the exposure to O_2 plasma (25 W) for 20 seconds to complete the cleaning process. The deposition area is typically 0.5 × 0.5 cm^2, patterned by nail-polish oil masking. We also performed deposition on copper foil (Alfa Aesar), Ni foam (Innovation Materials), carbon cloth, glassy carbon electrode (GCE), SiO_2/Si wafers, and glass. In a typical deposition, substrates were vertically placed in reaction mixtures of $KMnO_4$ and $Co(OAc)_2$ with 500 rpm stirring at 80 °C for 15 min. The subscript of CMOH represents the anions of cobalt precursors used in the deposition. CMOH without specific subscript refers to $Co(OAc)_2$-deposition. After the deposition, the coatings were rinsed with DI water and the nail-polish mask was removed with acetone. The CMOH annealing was carried out at 500 °C for 1 h under argon to obtain cobalt manganese oxide (CMO) films. The temperature-dependent CMOH deposition was carried out at room temperature, 50 °C, 80 °C, and 95 °C.

Reaction mixtures with varied Co/Mn mole ratios were prepared (Co : Mn = 1 : 3, 1 : 1, 3 : 1, 5 : 1, 7 : 1, and 9 : 1). For the redox deposition of iron manganese oxide coatings, we used $Fe(OAc)_2$ (Acros Organics) as the precursor with a Fe/Mn mole ratio of 3/1 in the reaction mixture. In the synthesis of ternary metal oxide films, $Co(OAc)_2$, $Fe(OAc)_2$, and $KMnO_4$ were mixed with a Fe/Co/Mn ratio of 1/2/1.

2.2. Electrochemical measurements

Electrochemical results were acquired using a three-electrode system on a CHI 614D Electrochemical Analyzer. FTO glass with CMOH coatings was used as the working electrode, where a Pt plate and Hg/HgO were used as the counter and reference electrodes, respectively. OER activities were evaluated by linear sweep voltammetry (LSV) with a scan rate of 5 mV s^{-1} under 0.1 M KOH. All the overpotentials (η) were recorded at 10 mA cm^{-2}. The potentials presented herein are based on the reversible hydrogen electrode (RHE) following the equation:[49]

$$E_{RHE} = E_{Hg/HgO} + 0.098 + 0.059 \times pH \quad (1)$$

Faradaic efficiency (FE) was obtained using a gas chromatograph (GC) equipped with a thermal conductivity detector (TCD) to analyze the quantity of molecular oxygen. The FE was acquired from the ratio of $O_{2\ measured}/O_{2\ theoretical}$, where $O_{2\ theoretical}$ was integrated from the current–time (i–t) curve. A quartz crystal microbalance (QCM/CHI 401) was used to monitor the *in situ* growth of CMOH coatings at room temperature. The fundamental resonant frequency of QCM is 8 MHz. The weight change was calculated using the Sauerbrey equation:

$$\Delta f = -(2 \times f_0^2 \times \Delta m)/[A(\rho_a \times G_a)^{1/2}] \quad (2)$$

where f_0 is the fundamental resonant frequency of QCM, ρ_a is the density of quartz (2.648 g cm^{-3}), G_a is the shear wave velocity of the quartz crystal (2.947 × 10^{11} g cm^{-1} s^{-2}), and A is the active electrode area of QCM. For all the QCM measurements, Au/quartz substrates were first kept in DI water until frequency equilibrium is reached. Afterwards, Co and Mn precursors were carefully injected into the system to initiate coating growth. Pure $Co(OAc)_2$ and $KMnO_4$ were also tested in QCM as control samples. To study the effect of counter ions, cobalt precursors with different anions of $Co(OAc)_2$, $CoSO_4$, and $Co(NO_3)_2$ were used following the same deposition conditions. Sodium acetate (Acros Organics) was used as the source of the acetate anion.

2.3. Characterization

Scanning electron microscopy (SEM) images were obtained using a FEI Inspect F50 and Zeiss Supra 55 Gemini with acceleration voltages of 10–20 kV. The X-ray photoelectron spectroscopy (XPS) measurements were done on a PHI 5000 VersaProbe. The film composition profile was studied by Ar-sputtering XPS with a removal rate of 3 nm min^{-1}. The grazing incident X-ray diffraction (GIXRD) was used to characterize CMOH thin coating with 1° grazing angle on a Bruker D8 Advance diffractometer with a CuKα X-ray source. Field

emission transmission electron microscopy (FE-TEM) images were collected with a FEI E.O Tecnai F20 G2 at 120 kV. TEM foils were prepared using a focused ion beam (FIB) using a SMI 3050. The CMOH/FTO samples were first coated with platinum and a subsequent carbon layer, followed by ion beam cutting and thinning. Samples were analyzed by energy dispersive X-ray spectroscopy (EDXS) under SEM and TEM. The Raman spectra were obtained using a WITec Confocal Raman Microscope with a 532 nm wavelength laser source. The CMOH samples were deposited on gold substrates to enhance the Raman signals *via* surface-enhanced Raman scattering. The X-ray absorption spectra (XAS) were collected at 17C1 in the National Synchrotron Radiation Research Center, Taiwan (NSRRC) with transmission mode. The roughness of CMOH films was analyzed by atomic force microscopy (AFM, Bruker Dimension Edge) with contact mode. The conductivity measurement was conducted using a four-point probe on a Quatek 5601Y Sheet Resistivity Meter. The UV-vis spectra were obtained with a Jasco V-630 UV-visible spectrometer. Inductively coupled plasma mass spectrometry (ICP-MS) measurements were carried out with a PerkinElmer ELAN 6100 DRC Plus for elemental analysis. To determine Co/Mn ratios, CMOH samples were dissolved in a solution composed of HNO_3 (60%) and H_2O_2 (35%) with a 2 : 1 volume ratio. To study the elemental leaching issue, the OER electrolyte solution (0.1 M KOH) after 10 000 cycle sweeps was sampled to determine the contents of Co and Mn.

2.4. Simulation of CMOH deposition behavior

Molecular dynamics (MD) simulations were carried out to investigate the growth of the CMOH film on the FTO surface. The cases of $Co(OAc)_2$ and $CoSO_4$ deposition were investigated. The composition of the MD cell in the acetate system includes 1500 Co^{2+}, 3000 OAc^-, 500 MnO_4^-, 500 K^+, and 2000 H_2O (solvent), while that of the sulfate system includes 1500 Co^{2+}, 1500 SO_4^{2-}, 500 MnO_4^-, 500 K^+, and 2000 H_2O. The crystalline tin oxide (SnO_2, 100 × 100 × 8 $Å^3$) substrate was established to imitate FTO glass for the deposition. All simulations were computed by using Material Studio software. COMPASS force field and NVT ensemble were adapted for the simulations.[50,51] The density of the liquid phase in each system was set to be 1.0 g cm^{-3}. The initial temperature of MD simulations was 298 K until a thermal equilibrium was reached; then the temperature was further increased to 353 K. This temperature setting corresponds to the real reaction temperature. The pair distances between Co^{2+} and Mn^{7+} (in MnO_4^-) to O on the SnO_2 surface, as well as Co^{2+} to O in MnO_4^- (*i.e.* (MnO_4)–Co complexes), were analyzed. The metal cation-to-O distances shorter than 3.0 Å were recognized to be due to the bond formation for yielding precipitate. This linking process was repeated five times for every 75 picoseconds.

3. Results and discussion

3.1. Deposition and characterization of CMOH coating

The solution processed deposition of binary CMOH films was carried out in a single-step redox process under ambient conditions. The aqueous reaction mixtures were prepared by dissolving various Co(II) precursors with $KMnO_4$ (as the metal-containing oxidant)[52] without any additives (*e.g.* organic solvents, surfactants, polymers, *etc.*). To clearly demonstrate film deposition, transparent FTO was selected as the substrate as shown in Fig. 1. The one-step CMOH deposition produced by the $Co(OAc)_2$ precursor (*i.e.* $CMOH_{acetate}$) can be accomplished by dipping pristine FTO in the reaction mixture, aging for a certain period of time, and removing it after complete deposition (Fig. 1a–c). Neither an inert atmosphere nor delicate operation was required. The uniformly dark contrast of deposition can be obtained with the homogeneous distribution of cobalt and manganese as proven by EDXS (Fig. S-1†). The ICP-MS analysis confirms the bulky composition of Co/Mn = 2.92 (Table 1), similar to the selected-area composition of 3.08 acquired by EDXS.

Compared to other solution-based depositions, homogeneous binary elemental distribution generally requires specific reaction conditions due to potential mismatch in properties (*e.g.* hydrolysis rates, K_{sp} constants, thermal stabilities, *etc.*) between precursors. The fixed electron exchange stoichiometry dependent on the redox synthesis provides a reliable composition homogeneity for multi-precursor deposition. Different from typical dip-coating or polymer-assisted deposition, our procedure does not need thermal annealing to eliminate organic/polymer components and to consolidate coating adhesion,[10] thus preserving the amorphous feature.

The SEM image (Fig. 1d) of the CMOH film deposited on a SiO_2 wafer shows the smooth and highly continuous coating with a root-mean-square (RMS) value of 3.16 nm as acquired using AFM (Fig. 1e). The GIXRD patterns of the samples deposited using $Co(OAc)_2$ and $CoSO_4$ precursors ($CMOH_{sulfate}$) show no diffraction peaks, indicating the amorphous features of CMOH coatings (Fig. 1f). The Raman spectra of $CMOH_{acetate}$ exhibit a broad band at 599 cm^{-1} (Fig. S-2†), which is also in agreement with the presence of amorphous cobalt oxide.[27] The signals of amorphous manganese oxide are difficult to recognize due to their relatively small amounts (<25%), significant peak broadening, and similar Raman wavenumbers to cobalt oxide.[34] By annealing $CMOH_{sulfate}$ at 500 °C for one hour, the coatings are shown to be crystalline corresponding to the spinel Co_3O_4 phase, denoted as cobalt manganese oxide ($CMO_{sulfate}$) (Fig. S-3†). To further verify the film crystallinity, the focused ion beam (FIB)-cut foils of $CMOH_{acetate}$ were characterized by high-resolution TEM. The TEM image of uncalcined $CMOH_{acetate}$ clearly shows amorphous features without any ordered lattice fringes (Fig. 1g and S-4†), in agreement with the amorphous deposition shown in Fig. 1f. The coating cross-section is highly continuous and pinhole/void-free with a major thickness of 6–10 nm, comparable with the thickness of 11 nm under AFM (Fig. S-5†). At this thickness, the reported coatings fabricated by physical deposition still remain discontinuous.[53] The annealed $CMO_{acetate}$ films exhibit crystalline lattices with a d-spacing of 0.244 nm, corresponding to the (311) plane of spinel Co_3O_4 (Fig. 1h).[54] The film conductivities are summarized in Table 2, showing that CMOH coatings exhibit the sheet resistance in the range of 7.4 × 10^7 to 13.0 × 10^7 (Ω $□^{-1}$). The

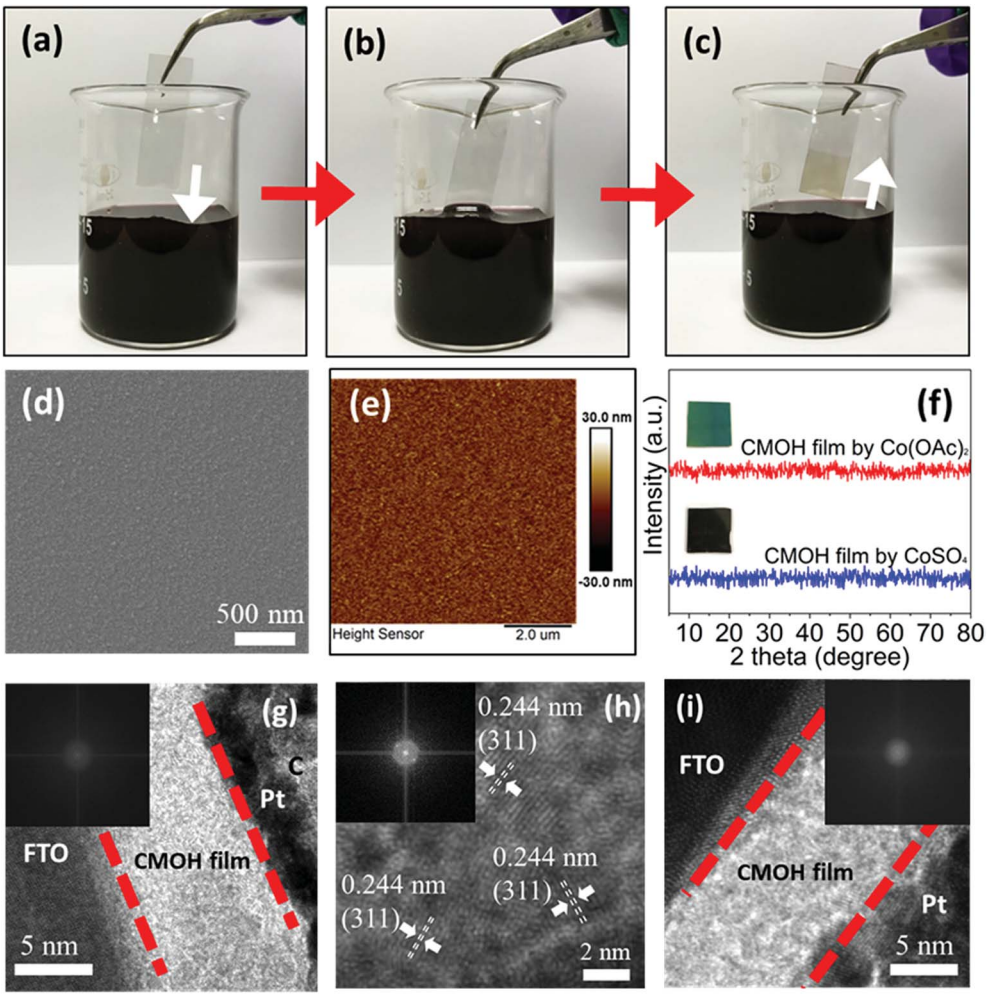

Fig. 1 Deposition procedure and characterization of $CMOH_{acetate}$. (a) Dipping a transparent FTO substrate into the aqueous reaction mixture of $Co(OAc)_2$ and $KMnO_4$, (b) aging FTO for 15 min, and (c) removing the FTO substrate after complete deposition (the darker contrast area). (d) The SEM image and (e) AFM data of the coatings. (f) The grazing-angle XRD patterns of thin and thick CMOH deposition by $Co(OAc)_2$ and $CoSO_4$, respectively. (g) The HR-TEM image of $CMOH_{acetate}$ foils, and (h) $CMO_{acetate}$ after annealed at 500 °C. (i) TEM image of CMOH after 10 000 cycles of OER tests. The insets in (g)–(i) are the corresponding Fourier transform patterns of the CMOH area.

annealed CMO generally displays a smaller sheet resistance (as low as $0.469 \times 10^7\ \Omega\ \square^{-1}$) than amorphous CMOH. $CMOH_{sulfate}$ is slightly more conductive than $CMOH_{acetate}$. Different Co/Mn ratios show insignificant influence on the film resistance. The controlled samples of manganese oxide coatings possess a sheet resistance that exceeds measurement limits,

Table 1 The elemental composition of CMOH films with varied deposition times and different precursor Co-to-Mn ratios

	Deposition time				
Co/Mn ratios of CMOH	1 min	5 min	15 min	30 min	60 min
	3.03	2.87	2.92	2.86	2.91
	Co(II)-to-Mn(VII) precursor ratios				
Co/Mn ratios of CMOH	3 : 1		5 : 1	7 : 1	9 : 1
	2.92		2.95	4.46	5.72

Table 2 The conductivity of CMOH and CMO coatings with varied divalent cobalt precursors and Co-to-Mn ratios

$Co(OAc)_2$-precursor coating	Sheet resistance ($\Omega\ \square^{-1}$) $\times 10^7$
Co : Mn = 3 : 1	13.0
Co : Mn = 7 : 1	11.5
Co : Mn = 3 : 1 (annealed)	10.6
Co : Mn = 7 : 1 (annealed)	8.95
$CoSO_4$-precursor coating	Sheet resistance ($\Omega\ \square^{-1}$) $\times 10^7$
Co : Mn = 3 : 1	7.41
Co : Mn = 7 : 1	7.40
Co : Mn = 3 : 1 (annealed)	0.470
Co : Mn = 7 : 1 (annealed)	0.469

suggesting that homogeneous binary oxide coatings exhibit a much lower sheet resistance than single oxides.

3.2. Large scale fabrication and properties of CMOH

With the easy operation procedure, we attempted to achieve high throughput fabrication by parallel dipping of numerous substrates in one batch of the reaction mixture. Fig. 2a and b show the success of parallel deposition to produce six individual, uniform and well-defined $CMOH_{acetate}$ coatings on FTO, more efficient than batch-to-batch deposition such as spin coating. In addition, shape- and size-specific deposition can be controlled by masking techniques. Fig. 2c shows the realization of large-scale arrays of square-shaped deposition over 10 × 10 cm^2 defined by the resin-based masks. All the patterned units of CMOH are well defined in shapes, interval distance, and show highly similar contrast. The scalable and throughput redox deposition appears highly practical for massive production.

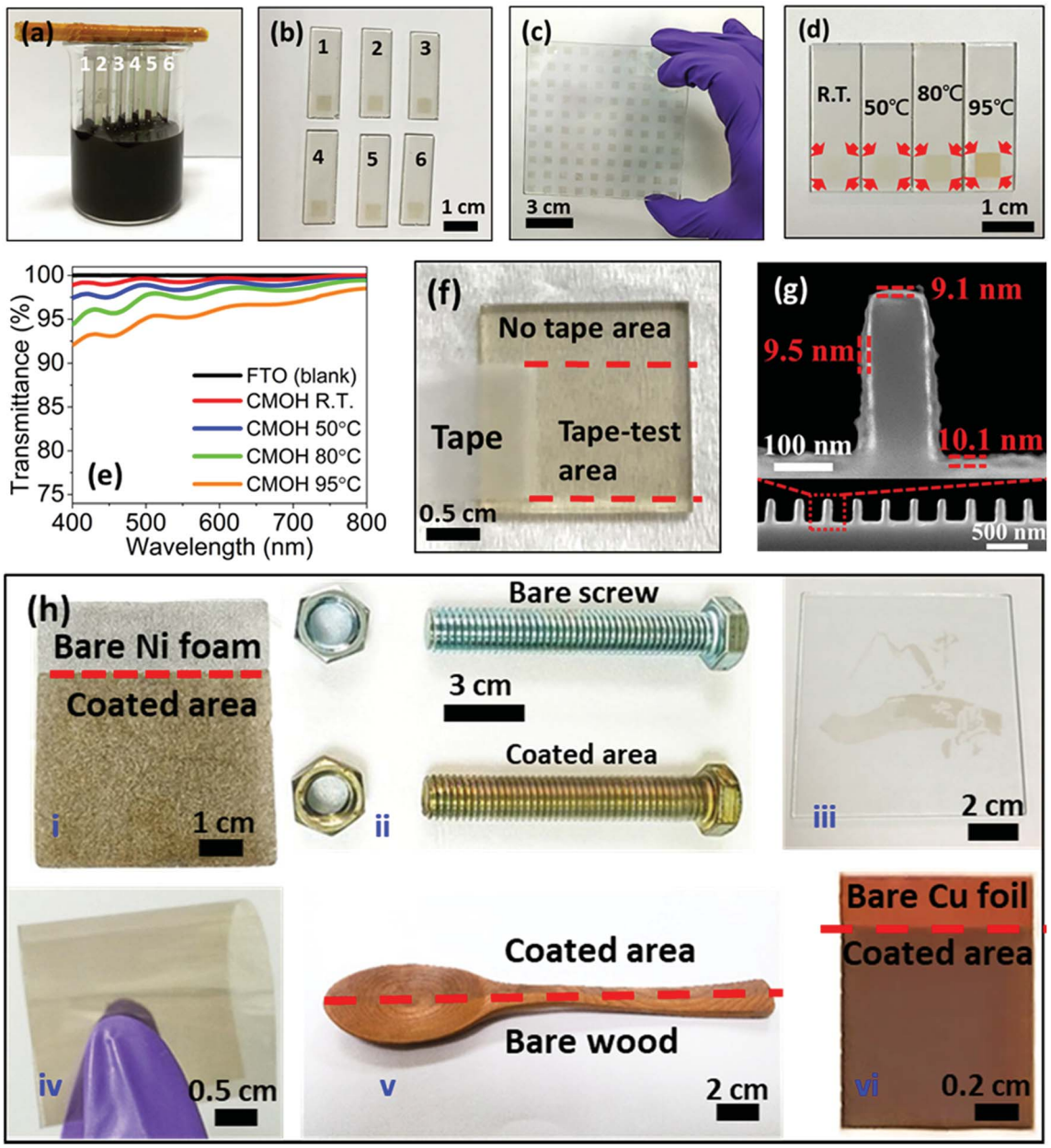

Fig. 2 Deposition condition tests. (a) The photographs of parallel deposition on six individual FTO substrates and (b) the products of six coated FTO films from (a) with uniform coating contrasts. (c) Large scale deposition of CMOH with a highly ordered array over a 100 cm^2 FTO film. (d) CMOH deposition at room temperature (R.T.) and others. The red arrows indicate the corners of the deposition areas. (e) The transparency of CMOH coatings shown in (d). (f) The CMOH adhesion tests by Scotch tape peeling for more than 100 cycles. (g) The cross-section profile of CMOH coating on a Si trench. (h) Tests of arbitrary substrate deposition: (i) CMOH coated on 3D porous Ni foam with the comparison of bare Ni foam; (ii) homogeneous deposition on the cylinder-shape surface of screw pairs; (iii) CMOH coating with transfer of large-size complicated patterns onto a 100 cm^2 glass substrate by masking. The CMOH coated PET (iv), where no appreciable cracking can be observed after bending and folding for 100 cycles; (v) the CMOH coated curved wooden surface; (vi) CMOH coated on the metallic surface of Cu foils.

Notably, the as-coated CMOH also exhibits high visible-light transparency. By changing the deposition temperatures (Fig. 2d), the coating contrasts become darker as the temperature increases indicating the formation of a thicker coating. The transparency (at 550 nm) of CMOH deposited at room temperature, 50 °C, 80 °C, and 95 °C was measured to be 99.2%, 98.4%, 97.4%, and 95.2%, respectively (Fig. 2e). Room-temperature CMOH forms a thin, uniform, and barely visible coating (see the arrows in Fig. 2d). This property becomes relevant as binary metal oxides recently gained attention as materials for transparent OER-active thin films.[55,56] Moreover, CMOH exhibits a higher transparency than the reported binary $FeNiO_x$ that is active for photoelectro-chemical cells (PEC) and sunlight-driven water splitting applications.[56]

Film adhesion is a crucial concern particularly for low-temperature deposition. As shown in Fig. 2f, we conducted peel-off tests with Scotch-tape on CMOH over 100 cycles. There were no appreciable film detachment or breaking observed. This strong adhesion is comparable to the annealed crystalline CMO samples, which allows CMOH to be directly used in the amorphous form. The step coverage studies show that CMOH coating can be deposited along the top, side wall, and base of SiO_2 trenches with a similar thickness of 9.1 nm, 9.5 nm, and 10.1 nm, respectively (Fig. 2g); hence, homogeneous CMOH deposition strongly attached on 3D complex architectures and porous tunnels can be expected.[57,58] As shown in Fig. 2h, we further successfully demonstrated CMOH deposition on complex 3D structures (Ni foam) and cylinder-shape substances (screw pairs). On different types of surfaces, including rigid glass, soft plastics (polyethylene terephthalate, PET), wood, and metal foils (Cu), CMOH deposition exhibits strong adhesion and high homogeneity (Fig. 2h). In particular, the coating on PET can completely tolerate the bending strain without appreciable film breaking after 100 cycle tests under 180° folding, agreeing with the excellent adhesion and mechanical properties.

3.3. Redox interaction

To verify the underlying principles of CMOH formation, oxidation states of cobalt and manganese are investigated. In the XPS spectra (Fig. 3a), the binding energy of Co $2p_{1/2}$ at 796.2 eV, $2p_{3/2}$ at 781.1 eV, and the satellite peaks at 790.8 eV reveals the presence of Co(III).[46] The XPS data also show that signals from Mn $2p_{3/2}$ and $2p_{1/2}$ are 641.8 and 654.2 eV, respectively, where Mn^{3+} and Mn^{4+} are barely distinguishable (Fig. 3b).[46] In the spectra of O 1s, the strong hydroxide signals can be observed at 532.0 eV and a weak signal of O^{2-} at 530.0 eV (Fig. 3c), showing similar ratios to metal oxyhydroxide species.[39] After film annealing at 500 °C, the hydroxide signals significantly decrease while O^{2-} signals are much stronger due to the conversion of amorphous oxyhydroxide to crystalline oxide (Fig. S-6†). Therefore, the presence of Co(III) and hydroxide/oxide signals indicates CoOOH-like amorphous CMOH.[46,52] We further conducted X-ray near edge structure studies of CMOH confirming the oxidation states of Co and Mn. The K-edge signals of Co (Fig. 3d) are observed at 7728.6 eV, corresponding to the reported octahedral-coordinated Co(III) at 7729 eV,[59] which further agrees with the XPS data. The Mn K-edge spectra (Fig. 3e) show the peak at 6563 eV, nearly identical to that of MnO_2 at 6562.2 eV instead of Mn(III) at 6554.2 eV.[60] The results, therefore, unambiguously confirm the presence of Co^{3+} and Mn^{4+} in CMOH coatings. As the elemental analysis highly agrees with ideal redox stoichiometry between Co^{2+} and Mn^{7+} as 3 : 1 (*i.e.* 2.86 to 3.03, see Table 1),[46] it is evident that the redox-driven CMOH deposition can be expressed as $Co_{1-x}Mn_{3x/4}OOH$. Therefore the net redox equation is shown as following:

$$9Co^{2+}{}_{(aq)} + 3MnO_4{}^{-}{}_{(aq)} + 14H_2O_{(l)} \rightarrow Co_9Mn_3O_{26}H_{13(s)} + 15H^{+}{}_{(aq)} \quad (3)$$

The film composition profiles of CMOH acquired by XPS (Fig. 3f) exhibit uniform Co : Mn mole ratios (*i.e.* 3.30 by

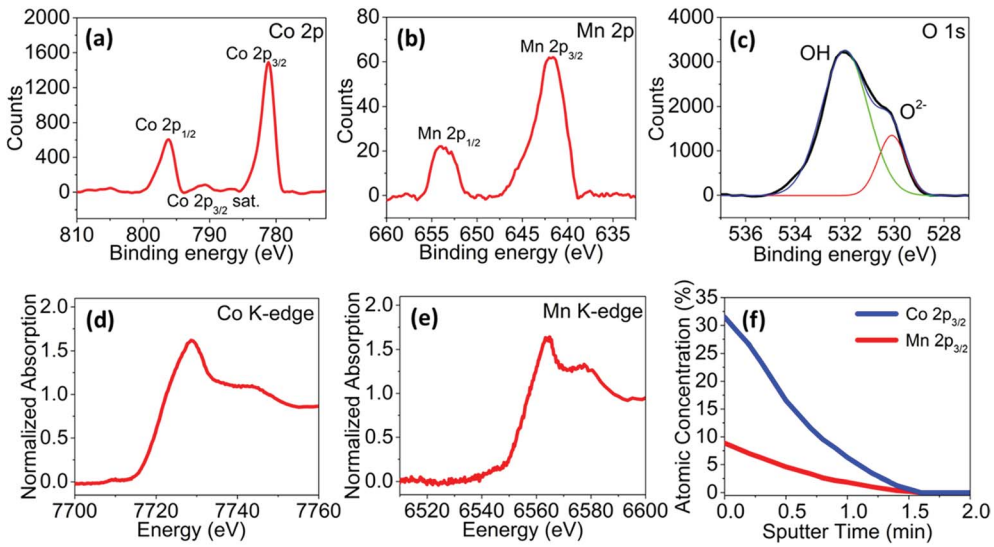

Fig. 3 Spectroscopic and profile studies of CMOH. The XPS data of (a) Co 2p, (b) Mn 2p, and (c) O 1s for uncalcined coating. The XAS spectra of (d) Co K-edge and (e) Mn K-edge. (f) The film composition profile.

average) from top to bottom, corresponding well with the redox-coupled film growth as shown in eqn (3). The depth profile studies show residue signals for sulfur and carbon to be less than 0.01%.

3.4. Coating formation process

We conducted QCM to monitor the loading mass and film growth of CMOH on Au/quartz substrates *in situ*.[11,56] First, we conducted control experiments of deposition with the precursor either $Co(OAc)_2$ or $KMnO_4$ only. The profiles of Fig. 4a show no increase of mass loading in the $Co(OAc)_2$-only case, while the appreciable film formation can be observed in the $KMnO_4$-only case. In addition, the deposition tests on carbon-based and transparent substrates also show that only $KMnO_4$-deposition contributes to film formation (see Fig. S-7†). This further confirms that the strong oxidative staining ability of $KMnO_4$ is critical for film formation and immobilization on substrates. For the tests combining $Co(OAc)_2$ and $KMnO_4$, the QCM profiles indicate a much faster and greater increase in mass loading than the previous two control experiments, verifying the redox-coupled nucleation.[52]

As Co^{2+} is the quantity-dominant species in the reaction mixture, attraction between the substrate-anchored MnO_4^- anion and Co^{2+} cation could facilitate on-site redox interaction on the substrate surface to form CMOH coating. Despite the reported studies of cobalt oxyhydroxide preparation *via* the redox route (*e.g.* interaction of Co^{2+} and $S_2O_8^{2-}$ to yield CoOOH),[54,61,62] their thin film deposition has been rarely recognized. Successful cobalt incorporation into the thin film form was first revealed in this work through redox interaction with $KMnO_4$. Theoretically, each Mn^{7+} would transfer charge directly to three neighboring Co^{2+} ions, giving the probability to construct interconnected networks holding multiple Co atoms with one Mn together through oxygen-bridged bonding. As a result, this network-like nucleation may favor the formation of continuous coating even at the ultrathin scale of several

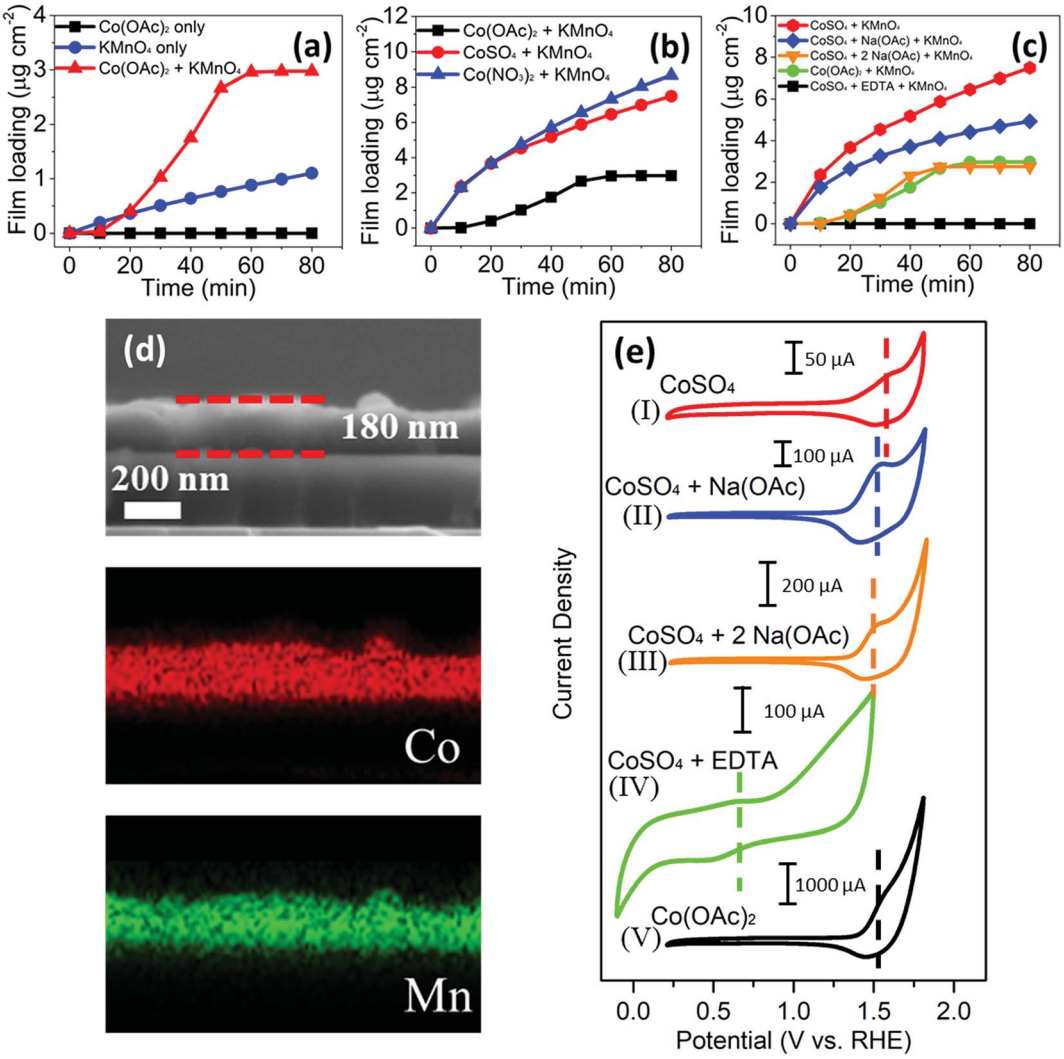

Fig. 4 The QCM studies of film growth with different precursor recipes. All the tests were conducted under identical preparation conditions. (a) The comparison of cobalt and manganese precursor-only cases with the two precursor mixed condition. (b) The comparison of different anions in the cobalt precursors. (c) The effect of additional ligands on CMOH growth. (d) The cross-sectional SEM image and EDXS mapping of CMOH prepared by $CoSO_4$. (e) The CVs of cobalt precursors with different anions and ligands.

nanometers, rather than island-like, discontinuous deposition frequently observed in physical vapor deposition. Therefore, $KMnO_4$ is proposed to play the dual roles of both a surface-anchoring oxidant and a cobalt-fixation reagent in the binary oxide deposition process.

3.5. Effect of the precursor anion on deposition

To investigate the control parameters of the film thickness, notably, we observed that film growth was highly dependent on the counterions of cobalt precursors. Under identical conditions, as shown in Fig. 4b, $CoSO_4$ and $Co(NO_3)_2$ precursors exhibit the general trend that the CMOH thickness is proportional to the deposition time. Their deposition rates (0.059 μg min^{-1} for $CoSO_4$ and 0.086 μg min^{-1} for $Co(NO_3)_2$) are 6 to 9 times faster than that for $Co(OAc)_2$ (0.0097 μg min^{-1}). In fact, the $CoSO_4$ and $Co(NO_3)_2$ deposition can continuously go beyond several hours to generate a much thicker coating. On the other hand, the $Co(OAc)_2$-deposition grew linearly at the first 50 min, and then became saturated at 60 min with the maximized loading mass of 2.97 μg cm^{-2} (Fig. 4b). This self-limiting phenomenon was also observed at different deposition temperatures of $CMOH_{acetate}$. The results clearly show that the deposition thicknesses produced vary depending on the precursor anions. As shown in Fig. 4d, the cross-sectional SEM image of $CMOH_{sulfate}$ for 2 hour deposition, featured with the homogeneous elemental distribution for 180 nm thickness with the absence of cracks or pinholes/voids. Together with the ultrathin thickness of $CMOH_{acetate}$, the film thickness can be controlled ranging from several nanometers up to submicrons *via* precursor anions. To lower the interfacial barrier of electrocatalysis, we adopted $Co(OAc)_2$ deposition to produce ultrathin $CMOH_{acetate}$ for the later OER studies.

To further investigate the effect of anions, we carried out the control experiments by adding acetate ions to $CoSO_4$-deposition (Fig. 4c). The addition of two acetate ion equivalents, whose quantity is comparable to that of $Co(OAc)_2$, yielded a nearly identical saturation time and coating mass to that of $Co(OAc)_2$-deposition. However, the addition of one acetate ion equivalent, which corresponds to half of that in $Co(OAc)_2$, behaved similar to that of $CoSO_4$-deposition but no saturation was observed. In addition, the loading mass lies in between those of $CoSO_4$ and $Co(OAc)_2$ deposition. These phenomena clearly indicate that the self-limiting film growth is due to the presence of the acetate anion. Morales-Guio *et al.*[56] also observed similar film growth inhibition with the identical anion combination of $Fe_2(SO_4)_3$ and $Ni(OAc)_2$ to our case. Indeed, acetate anions may act as a buffer species to influence the pH conditions and also the deposition. Their pH variation studies were partially effective but comprehensive understanding of the saturation growth of binary iron nickel oxides remained uncertain. Since the acetate anion possesses the stronger intrinsic coordination capability than the other two, it is most likely that the ligand coordination effect may rationalize the anion influence.

To verify the coordination effect, we added the hexadentate ligand of ethylenediaminetetraacetic acid (EDTA) as the much stronger coordination ligand than acetate for comparison. No coating formation can be observed in the presence of EDTA (Fig. 4c), indicating that its ability to coordinate with Co^{2+} significantly influences CMOH deposition. We therefore compared the oxidation potentials of EDTA- and acetate-coordinated Co(II) under the deposition conditions. The Co^{2+}/Co^{3+} oxidation potentials in the presence of acetate and sulfate anions are 1.55 and 1.63 V, respectively (Fig. 4e(I) and (V)). With the addition of the acetate ligand to Co sulfate (mole ratio 2 to 1, see Fig. 4e(II) and (III)), the Co^{2+}/Co^{3+} oxidation potentials decrease which is eventually similar to that of $Co(OAc)_2$. On the other hand, the addition of a stoichiometric amount of sodium sulfate to $Co(OAc)_2$ shows no significant change of Co^{2+} oxidation peaks. By adding EDTA to $CoSO_4$, a drastic decrease in the Co^{2+}/Co^{3+} oxidation potential to 0.67 V has been observed (Fig. 4e(IV)). This oxidation potential drop for Co^{2+} should make the redox deposition even easier and more spontaneous. But the observed absence of CMOH indicates that the ligand effect governs the deposition growth rather than the redox potential changes. The EDTA ligand traps Co^{2+} tightly and may keep the coordinated Co^{2+} away from the substrate for film growth. Compared to EDTA, the relatively labile and weak coordination of acetate may result in the suppressed deposition rather than a complete stop. It is also likely that the addition of coordination ligands may establish a new equilibrium unfavorable for the CMOH deposition. Thus, the precursor anion effect could be mainly attributed to the ligand coordination ability. As a result, the precise control of the thickness can be feasible through the proper selection of ligand additives.

3.6. Simulation study of CMOH growth

Fig. 5 shows the MD simulation studies of (MnO_4)–Co complexes that are yielded after the redox reaction in sulfate (Fig. 5a) and in acetate (Fig. 5b) deposition. The red, blue, and purple dots represent O, Co, and Mn, respectively. Two different (MnO_4)–Co complexes, one forms in solutions as a colloidal precipitate (Fig. 5c) while the other binds with SnO_2 substrates (Fig. 5d) as film deposition, were depicted and studied. The quantity of colloidal complexes in sulfate solution was observed to be larger than that in acetate solution. By correlating the numbers of (MnO_4)–Co colloidal complexes formed *versus* simulation time (Fig. 5g), it is found that the formation rates in the sulfate solution are more than those in the acetate solution. The saturated number of (MnO_4)–Co colloidal complexes in acetate solution is found to be 480. Since the total number of Co ions is 1500 at the initial stage, about one-third of Co ions in the acetate solution form the colloidal complexes. For ions in sulfate solution, the maximum number of colloidal complexes at the end of our simulation time is 780, that is, larger than one half of the number of Co ions.

Co ions are not only bonded to the oxygen in MnO_4, but also to the oxygen of the SnO_2 surface to form deposition (see Fig. 5e (sulfate system) and Fig. 5f (acetate system)). Similarly, the number of surface-linked complexes in sulfate solution was larger than that in acetate solution. Within the simulation time period, the number of surface-linked complexes in the acetate solution saturates but not in the sulfate case (Fig. 5h). These

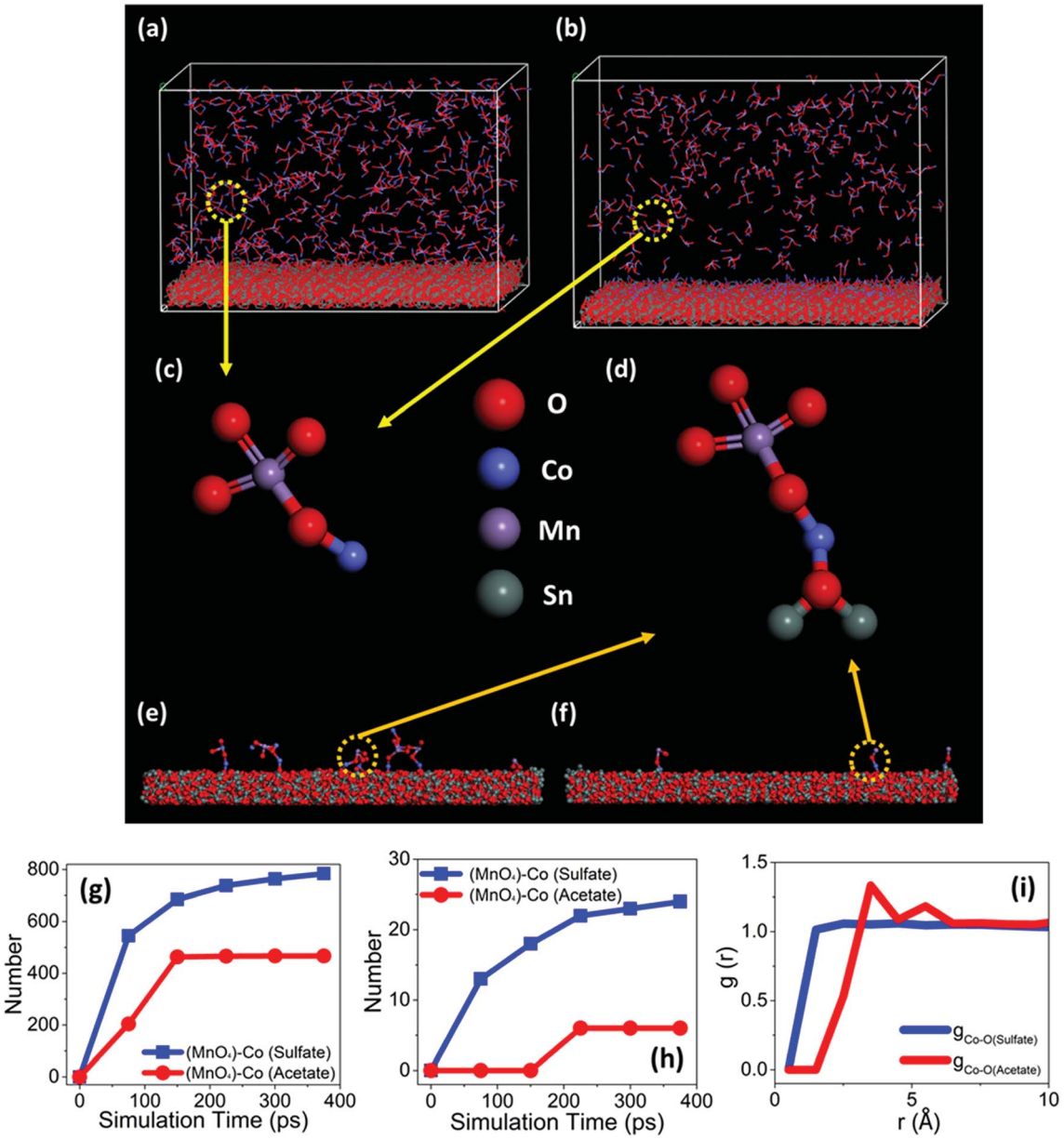

Fig. 5 The MD simulated studies of CMOH growth. The illustration of simulation cells of the (a) sulfate system and (b) acetate system while the simulation is in progress after linking. Removal of all the unreacted Co^{2+} and MnO_4^- ions, counter ions (OAc^-, SO_4^{2-}), and solvent (H_2O) was conducted to enable the clear presentation of (MnO_4)–Co complexes. (c) The enlarged view of a (MnO_4)–Co complex as a colloidal precipitate in cells (a) and (b). (d) The enlarged view of surface-linked (MnO_4)–Co complexes (CMOH film) deposited on the SnO_2 substrate in (e) the sulfate system and (f) the acetate system. (g) The numbers of Co–O–Mn bonds of the colloidal complexes, analyzed from cells of (a) and (b). (h) The numbers of Co–O–Mn bonds of the surface linked complexes, analyzed from (e) and (f). (i) The RDF analysis of Co^{2+} ions with O atoms of acetate ($O_{acetate}$) and sulfate ($O_{sulfate}$) ions.

simulation results agree well with the aforementioned experimental observation of ligand-governed CMOH deposition.

To further investigate the formation of the (MnO_4)–Co complex, we calculated the radial distribution function (RDF) of Co ions to O in sulfate ($g_{Co-O(sulfate)}$) and O in acetate ($g_{Co-O(acetate)}$). In Fig. 5i, $g_{Co-O(acetate)}$ has a peak appearing around 3.5 Å, while $g_{Co-O(sulfate)}$ has no corresponding peak. This means that acetate anions closely surround Co ions with a high local density rather than being homogeneously dispersed in the whole solution cell. Such acetate-ion aggregation restricts the coordination of Co^{2+} to other oxygen atoms (*e.g.* O of SnO_2 substrates), and may also accumulate a great negative charge barrier to repulse away the MnO_4^- anion from facilitating redox interaction. The significantly inhibited CMOH deposition can also be explained to be due to change in ligands, from acetate to EDTA.

3.7. Electrocatalysis of the OER

Fig. 6a shows a comparison of a linear sweep voltammogram (LSV) of amorphous $CMOH_{acetate}$ and crystalline $CMO_{acetate}$

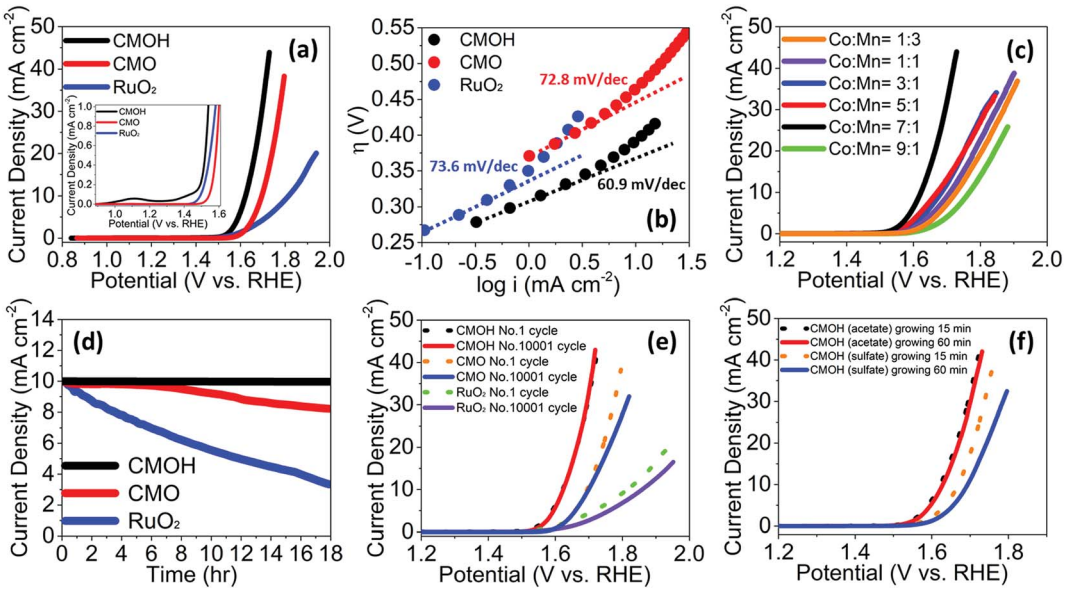

Fig. 6 Electrocatalytic oxygen evolution studies of CMOH coatings on FTO. (a) The comparison of amorphous CMOH and calcined CMO with benchmark RuO_2 recorded at 0.1 M KOH. Inset is the zoom-in plot. (b) Tafel plot comparison of materials in (a). (c) Current density–potential curves of CMOH coatings produced with varied Co-to-Mn ratios in the reaction mixtures. Stability comparison between amorphous and crystalline coatings in *i*–*t* curves (d) and LSV cycle tests (e). (f) The comparison of coatings with different cobalt precursors.

deposited on FTO under 0.1 M KOH. No appreciable OER activities can be observed with bare FTO up to 1.9 V. The OER onset and over potentials (η at 10 mA cm^{-2}) for amorphous CMOH are at 1.28 V and 390 mV, respectively. Crystalline CMO shows a higher onset potential than CMOH at 1.47 V with η of 460 mV. At an over potential of 400 mV, the current density of CMOH is 11.60 mA cm^{-2}, which is 4.7 times greater than that of CMO. As compared to benchmark RuO_2, CMOH has the smaller onset potential of 180 mV and an overpotential of 200 mV. In Fig. 6b, CMOH exhibits the favorable OER kinetics with a smaller Tafel slope of 60.9 mV dec^{-1} than that of CMO (72.8 mV dec^{-1}). The faradaic efficiency of CMOH was measured to be nearly 100%, indicating that no side electrochemical reaction occurred during the OER (Fig. S-8†). In general, the greater conductivities enable the higher electrocatalytic performance. Amorphous CMOH, despite its lower conductivity, exhibits higher OER performance as compared to crystalline CMO (Table 2), clearly showing the intrinsic OER superiority of amorphous materials over crystalline ones. The comparison of OER performance with the reported thin coating is summarized in Table S-1.†

Metal oxyhydroxide (*e.g.* CoOOH, NiOOH) has been identified as the activity species for the OER.[24,40,63] Thin amorphous metal oxyhydroxides are commonly obtained from the electrochemical conversion of metal hydroxides as pre-catalysts during the OER, rather than produced by direct deposition. Electrochemical conditioning is needed to transform crystalline metal hydroxides to oxyhydroxides for enhanced OER activity.[11] We found that no appreciable electrochemical conditioning was needed for CMOH to enhance OER performance (Fig. 6a) since it may be already in the form of oxyhydroxide.

To investigate the optimal composition, the coatings with varied Co/Mn ratios have been produced by changing the precursor ratios in the initial reaction mixtures (See Table 1). By increasing the contents of cobalt precursors, the coatings are generally produced with greater Co/Mn ratios. Due to the redox interaction, the Co/Mn ratios of coatings are shown to be less varied (*i.e.* 2.92–5.72) compared to those of the reaction mixtures ranging from 3/1 to 9/1. The Co/Mn precursor ratio of 7/1 yielded the most active coatings ($CMOH_{7/1}$) with the smallest onset potential among the others (Fig. 6c, S-9† and Table 3). The cobalt XPS data of $CMOH_{7/1}$ (Fig. S-10†) show a high similarity to those of $CMOH_{3/1}$, indicating that Co^{3+} is still the main species of the coatings, instead of Co^{2+}. This might also suggest that Co^{3+} is the active species responsible for the OER rather than Mn sites. Compared to the ideal redox stoichiometry and binary compositions, the relatively lower quantity of

Table 3 OER performance

	Electrochemical performance		
Sample	Onset potential (V)	Potential (V) @ 10 mA cm^{-2}	Tafel slope (mV dec^{-1})
Co : Mn = 1 : 3	1.50	1.73	64.0
Co : Mn = 1 : 1	1.47	1.71	62.9
Co : Mn = 3 : 1	1.43	1.68	62.0
Co : Mn = 5 : 1	1.41	1.67	61.2
Co : Mn = 7 : 1	1.28	1.62	60.9
Co : Mn = 9 : 1	1.45	1.77	77.8
CMO	1.47	1.69	72.8
RuO_2	1.42	1.82	73.6
CMOH/Nickel foam	1.23	1.54	80.1
CMOH/Cu foil	1.25	1.64	78.1
CMOH/Carbon cloth	1.36	1.57	68.9
CMOH/GCE	1.44	1.65	63.3

Mn in $CMOH_{7/1}$ may suggest Mn^{4+} substitution by Co^{3+} yielding cation vacancies in the framework of films due to charge compensation. These defects in small quantity could increase material conductivity and improve catalytic activities as those observed in $CMOH_{7/1}$ (see Table 2), but large contents of defects can weaken the structure stability.[64] The significant drop of activities at Co/Mn = 9/1 is thus attributed to the observed incomplete film formation due to even higher cation vacancies that collapse the framework of CMOH.

The OER stability tests of *i–t* curves (Fig. 6d) were conducted at a current density of 10 mA cm^{-2} for 60 000 seconds continuously. No appreciable drops (<2%) of current density for CMOH can be observed, while CMO shows the decrease of 18% of the current density. RuO_2 displays the more severe current density decrease of 67%, much larger than those of both CMOH and CMO. In addition, we compared cyclic LSV tests for 10 000 scans. Amorphous CMOH exhibits the nearly identical curves to the first run (Fig. 6e), while crystalline CMO shows the current density decay of 16% with the increase of overpotential by 16 mV. Benchmark RuO_2 exhibits even greater current density decay of 18% and an increase of overpotential by 44 mV after the tests. In fact, both CMOH and CMO can be more stable than RuO_2 over the whole cycle tests. In the TEM characterization, the CMOH after the 10 000 cycle tests still remains amorphous without any crystalline features (Fig. 1i), indicating that the exceptional oxygen evolution activities and stability were due to the amorphous characteristics despite the possible local structural rearrangement during the OER.

We further conducted leaching studies by sampling the OER electrolyte solutions (0.1 M KOH) after 10 000 cycles. The ICP-MS data show that crystalline CMO coatings release both Co and Mn twice more than amorphous CMOH, which may explain the poor stability of CMO compared to CMOH over time (Fig. 6d). The spinel phase has been recognized as an unfavorable structure to be transformed to oxyhydroxide.[11] Well-crystalline spinel CMO with a rigid, ordered coordination environment may restrict the flexibility of structural alteration. The high lattice stress due to phase transformation increases the probability of irreversible bond breaking, leading to the observed Co and Mn leach. In contrast, the disordered amorphous CMOH is more structurally flexible to tolerate the greater degrees of structural rearrangement, including $Co^{3+/4+}$ exchange in OER mechanisms.[16,37]

We studied the thickness effect on the OER by varying deposition time and with different precursors of $Co(OAc)_2$ and $CoSO_4$. As shown in Fig. 6f, under the same deposition time, the $Co(OAc)_2$-coatings generally exhibit better activities than $CoSO_4$-coatings. The nearly identical OER activities between 15 min and 60 min $Co(OAc)_2$-coatings consist of the observed self-limiting growth and negligible difference in thickness (also see Fig. S-11†). For the case of $CoSO_4$-coatings, the longer deposition time results in the weaker OER performance closely associated with their drastic thickness difference. As ultrathin coating facilitates charge transport in electrocatalysis, the thickness control of CMOH through the ligand coordination effect can be a promising route to manipulate OER performance.

3.8. OER on various substrates

With the substrate-universal deposition and easy operation, we tested ultrathin CMOH on various substrates commonly used

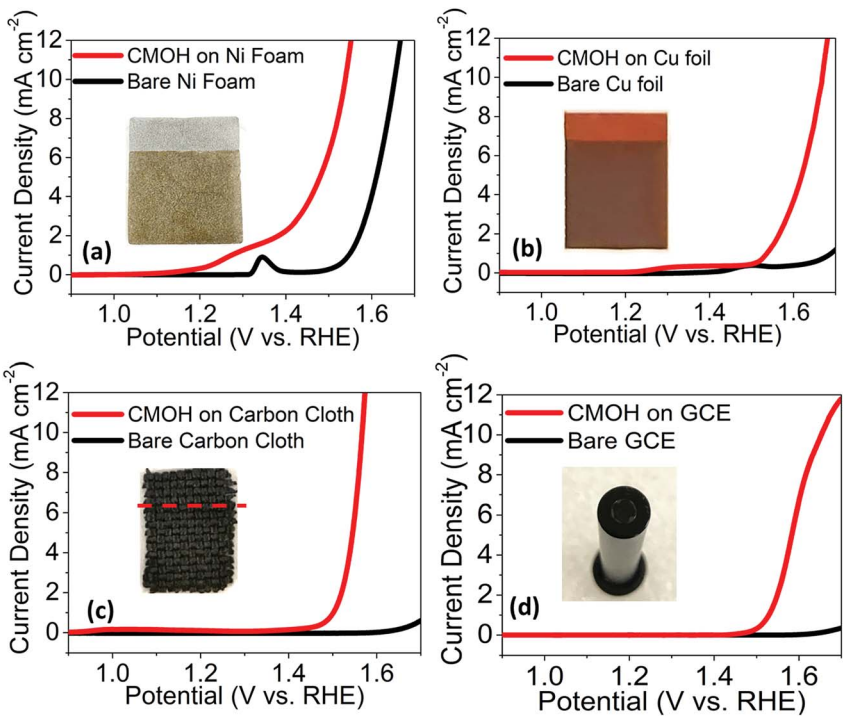

Fig. 7 Current density–potential curve comparison of amorphous CMOH coated on typical substrates for the OER: (a) Ni foam, (b) Cu foils, (c) carbon cloth, and (d) glassy carbon electrode (GCE).

for the OER, including metal foils (Cu foils), carbon cloth, 3D Ni foams, and a glassy carbon electrode (GCE).[16,57,65,66] As shown in Fig. 7, the electrochemical results generally show the superior OER enhancement compared to the uncoated substrates, suggesting (1) the strong interfacial contacts between CMOH and the substrates for electrocatalysis, and (2) the exceptional OER activity of amorphous CMOH coatings. Notably, the LSV curve for bare Ni foam shows the oxidation peak at 1.34 V, corresponding to the transformation of Ni(II)/(III).[57] However, the CMOH coating on Ni foam does not reflect the Ni(II)/(III) signal, but it exhibits an OER onset potential of 1.234 V which is very close to the theoretical one (1.23 V) together with a small overpotential of 0.31 mV. The improved OER performance has been summarized in Table 3. Under a 3 V electrolysis setup made by a series connection of two commercial batteries (1.5 V for each), the operation video clips (see ESI†) show vigorous O_2 bubbling solely from the CMOH coated area rather than the uncoated ones. Compared to CMOH-coated electrodes, the commercial pristine carbon rods and Pt wires are relatively weaker in O_2 production under the same conditions. These results confirm that CMOH is responsible for the oxygen evolution with the superior OER activity to the substrates, including highly conductive and electrocatalytically active copper foils and Ni foam.

3.9. Ternary oxide film deposition

Following the deposition principle above, we explored diverse film compositions by replacing Co^{2+} with other transition metals, such as Fe^{2+}. The preliminary results show the success of iron manganese oxide coatings with a Fe/Mn ratio of 2.39, suggesting the feasibility of various metal oxide combinations through the redox protocol. Furthermore, with the presence of both Co^{2+} and Fe^{2+} with $KMnO_4$, the ternary iron-cobalt-manganese oxide coatings on FTO have been successfully produced, in which their component ratios are similar to the precursor ratios (Fe : Co : Mn = 1 : 2.11 : 0.77, see Fig. S-12†). The metal ion fixation role of $KMnO_4$ has been observed again for both Co^{2+} and Fe^{2+}. According to previous work, metal-containing oxidant $KMnO_4$ in the redox synthesis can potentially be replaced by other oxometallates (*i.e.* $K_2Cr_2O_7$),[52] not limited to $KMnO_4$ only. The realization of diverse combinations of multi-component amorphous coatings can be thus systematically studied *via* this redox protocol.

4. Conclusion

We reported the scalable, solution-processable protocols for multicomponent ultrathin metal oxide coatings capable of achieving pinhole-free, continuous, and substrate universal deposition. The redox-coupled film formation was proved critical for film growth, fixation, and homogeneous elemental distribution. As there is no more need for pyrolysis treatment, this protocol is a suitable alternative for amorphous deposition and substrates with low thermal durability. CMOH thickness and compositions can be controlled by means of ligand selection. This protocol might be useful for the fabrication of wearable semiconductor devices, such as gate material deposition. For oxygen evolution, the new exploration of multi-component amorphous metal oxides (*e.g.* more than four different metals) can be pursued for even greater durability and efficiency. The high transparency and film integrity by the redox protocol may open a new avenue for light-assisted PEC applications.

Conflicts of interest

There are no conflicts to declare.

Acknowledgements

We acknowledge the financial support from the Ministry of Science and Technology, Taiwan under grant 106-2113-M-110 -010. We also thank Professor Yuan-Chieh Tseng for his support for X-ray absorption spectroscopy. We thank Professor Cheng-Lung Chen for MD simulation studies. We thank Professor Yung-Jr Hung for the supply of SiO_2 trenches on wafers.

References

1 F. Lin and S. W. Boettcher, *Nat. Mater.*, 2014, **13**, 81–86.
2 C. Glynn and C. O'Dwyer, *Adv. Mater. Interfaces*, 2017, **4**, 1600610.
3 S. Y. Reece, J. A. Hamel, K. Sung, T. D. Jarvi, A. J. Esswein, J. J. H. Pijpers and D. G. Nocera, *Science*, 2011, **334**, 645–648.
4 J. S. Mondschein, J. F. Callejas, C. G. Read, J. Y. C. Chen, C. F. Holder, C. K. Badding and R. E. Schaak, *Chem. Mater.*, 2017, **29**, 950–957.
5 K. L. Pickrahn, S. W. Park, Y. Gorlin, H.-B.-R. Lee, T. F. Jaramillo and S. F. Bent, *Adv. Energy Mater.*, 2012, **2**, 1269–1277.
6 T. Tian, L. Huang, L. Ai and J. Jiang, *J. Mater. Chem. A*, 2017, **5**, 20985–20992.
7 C. Qiu, L. Ai and J. Jiang, *ACS Sustainable Chem. Eng.*, 2018, **6**, 4492–4498.
8 M. Wang, J. Jiang and L. Ai, *ACS Sustainable Chem. Eng.*, 2018, **6**, 6117–6125.
9 J. He, D. M. Weekes, W. Cheng, K. E. Dettelbach, A. Huang, T. Li and C. P. Berlinguette, *J. Am. Chem. Soc.*, 2017, **139**, 18174–18177.
10 Q. X. Jia, T. M. McCleskey, A. K. Burrell, Y. Lin, G. E. Collis, H. Wang, A. D. Q. Li and S. R. Foltyn, *Nat. Mater.*, 2004, **3**, 529–532.
11 L. Trotochaud, J. K. Ranney, K. N. Williams and S. W. Boettcher, *J. Am. Chem. Soc.*, 2012, **134**, 17253–17261.
12 R. D. L. Smith, M. S. Prévot, R. D. Fagan, Z. Zhang, P. A. Sedach, M. K. J. Siu, S. Trudel and C. P. Berlinguette, *Science*, 2013, **340**, 60–63.
13 M. B. Stevens, L. J. Enman, A. S. Batchellor, M. R. Cosby, A. E. Vise, C. D. M. Trang and S. W. Boettcher, *Chem. Mater.*, 2017, **29**, 120–140.
14 G. Saat, F. M. Balci, E. P. Alsaç, F. Karadas and Ö. Dag, *Small*, 2018, **14**, 1701913.

15 L. Ai, J. Su, M. Wang and J. Jiang, *ACS Sustainable Chem. Eng.*, 2018, **6**, 9912–9920.
16 Y. Pei, Y. Yang, F. Zhang, P. Dong, R. Baines, Y. Ge, H. Chu, P. M. Ajayan, J. Shen and M. Ye, *ACS Appl. Mater. Interfaces*, 2017, **9**, 31887–31896.
17 W. Zhang, Y. Wu, J. Qi, M. Chen and R. Cao, *Adv. Energy Mater.*, 2017, **7**, 1602547.
18 C. G. Morales-Guio, L. Liardet and X. Hu, *J. Am. Chem. Soc.*, 2016, **138**, 8946–8957.
19 W. Liu, K. Du, L. Liu, J. Zhang, Z. Zhu, Y. Shao and M. Li, *Nano Energy*, 2017, **38**, 576–584.
20 J. Qi, W. Zhang and R. Cao, *Adv. Energy Mater.*, 2018, **8**, 1701620.
21 I. Roger, M. A. Shipman and M. D. Symes, *Nat. Rev. Chem.*, 2017, **1**, 0003.
22 I. Roger and M. D. Symes, *J. Mater. Chem. A*, 2016, **4**, 6724–6741.
23 B. M. Hunter, H. B. Gray and A. M. Müller, *Chem. Rev.*, 2016, **116**, 14120–14136.
24 M. S. Burke, L. J. Enman, A. S. Batchellor, S. Zou and S. W. Boettcher, *Chem. Mater.*, 2015, **27**, 7549–7558.
25 S. F. Hung, Y. Y. Hsu, C. J. Chang, C. S. Hsu, N. T. Suen, T. S. Chan and H. M. Chen, *Adv. Energy Mater.*, 2018, **8**, 1701686.
26 L. Gong, X. Y. E. Chng, Y. Du, S. Xi and B. S. Yeo, *ACS Catal.*, 2018, **8**, 807–814.
27 Z. Chen, L. Cai, X. Yang, C. Kronawitter, L. Guo, S. Shen and B. E. Koel, *ACS Catal.*, 2018, **8**, 1238–1247.
28 K. Zhang, T. Dong, G. Xie, L. Guan, B. Guo, Q. Xiang, Y. Dai, L. Tian, A. Batool, S. U. Jan, R. Boddula, A. A. Thebo and J. R. Gong, *ACS Appl. Mater. Interfaces*, 2017, **9**, 42723–42733.
29 P. Babar, A. Lokhande, H. H. Shin, B. Pawar, M. G. Gang, S. Pawar and J. H. Kim, *Small*, 2018, **14**, 1702568.
30 M. Huynh, C. Shi, S. J. L. Billinge and D. G. Nocera, *J. Am. Chem. Soc.*, 2015, **137**, 14887–14904.
31 S. W. Lee, C. Carlton, M. Risch, Y. Surendranath, S. Chen, S. Furutsuki, A. Yamada, D. G. Nocera and Y. Shao-Horn, *J. Am. Chem. Soc.*, 2012, **134**, 16959–16962.
32 E. R. Young, D. G. Nocera and V. Bulovic, *Energy Environ. Sci.*, 2010, **3**, 1726–1728.
33 E. Davari, A. D. Johnson, A. Mittal, M. Xiong and D. G. Ivey, *Electrochim. Acta*, 2016, **211**, 735–743.
34 A. Ramírez, P. Hillebrand, D. Stellmach, M. M. May, P. Bogdanoff and S. Fiechter, *J. Phys. Chem. C*, 2014, **118**, 14073–14081.
35 C.-C. Hou, Q.-Q. Chen, C.-J. Wang, F. Liang, Z. Lin, W.-F. Fu and Y. Chen, *ACS Appl. Mater. Interfaces*, 2016, **8**, 23037–23048.
36 M. W. Kanan and D. G. Nocera, *Science*, 2008, **321**, 1072–1075.
37 A. Bergmann, E. Martinez-Moreno, D. Teschner, P. Chernev, M. Gliech, J. F. de Araújo, T. Reier, H. Dau and P. Strasser, *Nat. Commun.*, 2015, **6**, 8625.
38 M. Risch, F. Ringleb, M. Kohlhoff, P. Bogdanoff, P. Chernev, I. Zaharieva and H. Dau, *Energy Environ. Sci.*, 2015, **8**, 661–674.
39 J. Y. Kim, D. H. Youn, K. Kang and J. S. Lee, *Angew. Chem., Int. Ed.*, 2016, **55**, 10854–10858.
40 J. Masa, P. Weide, D. Peeters, I. Sinev, W. Xia, Z. Sun, C. Somsen, M. Muhler and W. Schuhmann, *Adv. Energy Mater.*, 2016, **6**, 1502313.
41 Y. Zhang, T. Gao, Z. Jin, X. Chen and D. Xiao, *J. Mater. Chem. A*, 2016, **4**, 15888–15895.
42 R. D. L. Smith, M. S. Prévot, R. D. Fagan, S. Trudel and C. P. Berlinguette, *J. Am. Chem. Soc.*, 2013, **135**, 11580–11586.
43 H. Kim, J. Park, I. Park, K. Jin, S. E. Jerng, S. H. Kim, K. T. Nam and K. Kang, *Nat. Commun.*, 2015, **6**, 8253.
44 R. D. L. Smith, C. Pasquini, S. Loos, P. Chernev, K. Klingan, P. Kubella, M. R. Mohammadi, D. Gonzalez-Flores and H. Dau, *Nat. Commun.*, 2017, **8**, 2022.
45 D. González-Flores, I. Sánchez, I. Zaharieva, K. Klingan, J. Heidkamp, P. Chernev, P. W. Menezes, M. Driess, H. Dau and M. L. Montero, *Angew. Chem., Int. Ed.*, 2015, **54**, 2472–2476.
46 C.-C. Kuo, W.-J. Lan and C.-H. Chen, *Nanoscale*, 2014, **6**, 334–341.
47 M. B. Stevens, C. D. M. Trang, L. J. Enman, J. Deng and S. W. Boettcher, *J. Am. Chem. Soc.*, 2017, **139**, 11361–11364.
48 Z. Wu, X. Wang, J. Huang and F. Gao, *J. Mater. Chem. A*, 2018, **6**, 167–178.
49 W.-Y. Kao, W.-Q. Chen, Y.-H. Chiu, Y.-H. Ho and C.-H. Chen, *Sci. Rep.*, 2016, **6**, 37174.
50 H. Sun, *J. Phys. Chem. B*, 1998, **102**, 7338–7364.
51 P.-H. Chuang, Q. Gu, Y.-H. Tseng and C.-L. Chen, *J. Colloid Interface Sci.*, 2014, **417**, 310–316.
52 W.-J. Lan, C.-C. Kuo and C.-H. Chen, *Chem. Commun.*, 2013, **49**, 3025–3027.
53 C.-W. Huang, J. A. A. Valinton, Y. Hung Jr and C.-H. Chen, *Sens. Actuators, B*, 2018, **266**, 463–471.
54 C.-Y. Su, W.-J. Lan, C.-Y. Chu, X.-J. Liu, W.-Y. Kao and C.-H. Chen, *Electrochim. Acta*, 2016, **190**, 588–595.
55 A. Azarpira, J. Pfrommer, K. Olech, C. Hohn, M. Driess, B. Stannowski, T. Schedel-Niedrig and M. Lublow, *J. Mater. Chem. A*, 2016, **4**, 3082–3090.
56 C. G. Morales-Guio, M. T. Mayer, A. Yella, S. D. Tilley, M. Grätzel and X. Hu, *J. Am. Chem. Soc.*, 2015, **137**, 9927–9936.
57 T. Tang, W.-J. Jiang, S. Niu, N. Liu, H. Luo, Y.-Y. Chen, S.-F. Jin, F. Gao, L.-J. Wan and J.-S. Hu, *J. Am. Chem. Soc.*, 2017, **139**, 8320–8328.
58 X. Lu and C. Zhao, *Nat. Commun.*, 2015, **6**, 6616.
59 B. Das, M. V. Reddy and B. V. R. Chowdari, *Nanoscale*, 2013, **5**, 1961–1966.
60 W. Zhang, Z. Zhang, S. Kwon, F. Zhang, B. Stephen, K. K. Kim, R. Jung, S. Kwon, K.-B. Chung and W. Yang, *Appl. Catal., B*, 2017, **206**, 271–281.
61 C.-H. Chen, S. F. Abbas, A. Morey, S. Sithambaram, L.-P. Xu, H. F. Garces, W. A. Hines and S. L. Suib, *Adv. Mater.*, 2008, **20**, 1205–1209.
62 C. K. King'ondu, A. Iyer, E. C. Njagi, N. Opembe, H. Genuino, H. Huang, R. A. Ristau and S. L. Suib, *J. Am. Chem. Soc.*, 2011, **133**, 4186–4189.

63 M. S. Burke, M. G. Kast, L. Trotochaud, A. M. Smith and S. W. Boettcher, *J. Am. Chem. Soc.*, 2015, **137**, 3638–3648.
64 C.-H. Chen, E. C. Njagi, S.-Y. Chen, D. T. Horvath, L. Xu, A. Morey, C. Mackin, R. Joesten and S. L. Suib, *Inorg. Chem.*, 2015, **54**, 10163–10171.
65 J. W. D. Ng, M. García-Melchor, M. Bajdich, P. Chakthranont, C. Kirk, A. Vojvodic and T. F. Jaramillo, *Nat. Energy*, 2016, **1**, 16053.
66 S. Han, S. Liu, R. Wang, X. Liu, L. Bai and Z. He, *ACS Appl. Mater. Interfaces*, 2017, **9**, 17186–17194.